Fracture Parameter Investigations of Functionally Graded Materials by Using Ordinary State Based Peridynamics

Hanlin Wang[a], Satoyuki Tanaka[a], Selda Oterkus[b], Erkan Oterkus[b]

[a] *Graduate School of Advanced Science and Engineering, Hiroshima University, Japan,*
e-mail: hanlinwang@hiroshima-u.ac.jp; satoyuki@hiroshima-u.ac.jp.
[b] *Department of Naval Architecture, Ocean and Marine Engineering,*
University of Strathclyde, United Kingdom.
e-mail: selda.oterkus@strath.ac.uk; erkan.oterkus@strath.ac.uk.

Abstract

Static and dynamic fracture parameter analyses of functionally graded materials (FGMs) are conducted by using the ordinary state based peridynamic theory (OSPD). As a meshfree method, OSPD applies an integral equation to describe the motion of objects, avoiding the geometrical singularity in conventional fracture analysis measures. Domain integral method by introducing material gradient terms is employed in evaluating the static and dynamic stress intensity factors (SIFs). Meanwhile, peridynamic differential operator (PDDO) is also applied for the calculation of physical components derivatives. Different FGM modeling schemes are also examined in the OSPD framework. Cracked FGM structures with mode-I and mixed-mode crack scenarios are under investigation and results are validated by reference solutions. Accuracy and reliability of the proposed method will be examined and discussed.

Keywords: Ordinary state based peridynamics, Peridynamic differential operator, Interaction integral, Fracture analysis, Stress intensity factor

Nomenclature

A	Area enclosed by contours Γ_0, Γ and crack surfaces
a	Crack length
A_0	Area enclosed by contour Γ_0 and crack surfaces
a_1, b, d	OSPD parameters
$\boldsymbol{b}_i$	Body force density of material point i
C_{d}	Longitudinal wave speed
$C_{ijkl}(x)$	Spatially varied constitutive tensor
$E, E(x)$	Elastic modulus
E_0	Elastic modulus on x=0
$f(\boldsymbol{x}_i)$	Arbitrary physical function on point i
$g_2^{p_1 p_2}$	2D PD function
h	Plate thickness
H_x	Horizon
J	J-integral value
$K_{\mathrm{I}}, K_{\mathrm{II}}$	Mode-I and -II SIFs
$K_{\mathrm{I}}^*, K_{\mathrm{II}}^*$	Normalized mode-I and -II SIFs
$l_{\mathrm{I}}, l_{\mathrm{II}}$	Functions for analytical solutions of crack tip displacement field on mode-I and -II
$m(\boldsymbol{x}_i, \boldsymbol{x}_i, t)$	Bond connection indicator of point i
N	Total number of material points in PD model
n	Total number of material points in the horizon
n_j'	Unit normal vector on the J-integral contour
P_{avg}	Average material properties on bond
P_i	Material properties on point i
$q, q_{,j}$	q-function and its spatial derivatives
R	Remainder terms in Taylor Series
r	Distance to crack tip
r'	Hole radius
r_{d}	Contour size of interaction integral
s_{ij}	Bond stretch
s_c	Critical bond stretch
t	Computing time
t^*	Normalized computing time
$\boldsymbol{t}_{ij}$	Force state of point i
$\boldsymbol{u}_i$	Displacement vector of point i
$\ddot{\boldsymbol{u}}_i$	Acceleration vector of point i
u_i	Displacement components
$u_{i,j}$	Partial derivatives of displacement components over j-coordinate
$\ddot{u}_i$	Derivatives of displacement components over time
V_i	Volume of point i

W_i	Strain energy density of point i	Θ_i	Dilatation term of point i
x, y	Global coordinates	λ, μ	Lamé's constants
x', y'	Local coordinates	ν	Poisson's ratio
$\boldsymbol{x}_i, \boldsymbol{x}_j$	Initial configuration of points i and j	ξ_1, ξ_2	x- and y-component of bond
$\boldsymbol{y}_i, \boldsymbol{y}_j$	Deformed configuration of points i and j	$\rho_i(\boldsymbol{x})$	Spatially varied mass density
Γ, Γ_0	Outer and inner J-integral contours	ρ_0	Mass density on x=0
β_1, β_2	Coefficients of material property gradient	σ_{ij}	Cauchy stress components
δ	Horizon size	$\sigma_t(x)$	Stress loading function
δ_{ij}	Kronecker delta	$\Phi(\boldsymbol{x}_i)$	Damage value of point i
ε_{ij}	Strain components	ϕ	Inclined angle in local coordinate system
Δx	Grid spacing	ψ	Crack inclined angle
θ	Angle between horizontal axis and bond	ω_f	Weight coefficient for FGM modeling
		ω_{ij}	Weight function for PD

1. Introduction

With rapid development of modern industries, homogeneous materials may not always satisfy the high requirements of engineering practices. Therefore, a combination of multiple materials in solid state is invented by synthesis technologies, which is known as composite materials. FGM, as a new class of composite material, is composed of multi-phase material with pre-defined fractions of constituents varying gradually throughout a structure. Hence, it leads to continuous varying material properties in the structure. Due to this unique characteristics, FGM has shown its promising potential in aerospace [1], biomaterial [2], military defence [3] and electronics [4]. In many applications, such as, thermal barrier coating and nuclear fast breeder reactor, structures with FGM are usually accompanied with extreme loadings during operation. They have posed challenges for FGM in terms of stiffness, strength and stability. As one kind of heterogeneous materials, the micro-structure of FGM may be more complex than homogeneous materials. Therefore, the

integrity and toughness of FGM under various type of loadings are of vital importance.

Fracture analyses about FGM have been elaborately conducted during past decades. Erdogan and Wu [5] had proposed an analytical method in research of edge-cracked FGM strip. The relationships among SIF, loading condition and material variation are discussed in detail. Zhong and Cheng [6] applied the Fourier transform in the analysis of plane elasticity problem for cracked strip with FGM. They found out that the graded variation of elastic modulus can substantially improve the material fracture toughness. Based on Fourier transform, Shodja and Ghahremaninejad [7] studied the performance of FGM coating under mechanical and thermal stresses due to the Hertzian surface pressure. Guo and Noda [8] investigated the relationship between crack position and SIF for two-layer FGM structure with different material properties in each layer. By using integral transform, they concluded that once the crack tip lies on the interface of layers, SIF will reach extreme values as compared with other cracked cases.

Analytical approaches, as shown above, usually provide highly accurate solutions but complicated solution methods are necessary. For problems with complex geometries and boundary conditions, it might be unrealistic to obtain the analytical solutions. With rapid development of computing technologies, many numerical methods are applied in solution approximation. Yao et al. [9] applied optical caustics method to experimentally investigate dynamic fracture behaviour of FGM and the results were validated by finite element method (FEM). They found out that the crack initiation and propagation strongly depend on the elastic gradient around crack tip. Song and Paulino [10] applied the domain integral method in calculating the dynamic stress intensity factors (DSIFs) of structure with heterogeneous materials based on FEM. The static domain integral equations were extended to incorporate the dynamic effects and non-homogeneity with good accuracy. Anlas et al. [11] evaluated the SIF of edge-cracked FGM plate by using J-integral based on FEM. Kim and Paulino [12] used J-integral, modified crack closure integral and displacement correlation methods to evaluate the mixed-mode SIFs on FGM based on FEM. Zhang et al. [13] proposed a boundary integral equation method (BIEM) in the dynamic analysis of infinite FGM domain with finite crack. They pointed out that the DSIFs may be significantly influenced by materials gradients. Dolbow and Gosz [14] revisited some benchmark fracture problems by using interaction integral based on extend finite element method (XFEM).

The numerical simulation techniques mentioned above can be categorized within the framework of classical continuum mechanics (CCM). In CCM, structure or problem domains are assumed to be continuous which allows the employment of partial differential equations (PDEs) in describing the motion. However, damage and fracture are discontinuous in their nature and it will bring mathematical difficulties to the methods based on CCM. For dynamic fracture behaviour, especially crack initiation and propagation, geometrical singularity might have negative effects on the efficiency and accuracy of these numerical simulation techniques. In consideration of this situation, many meshfree methods are proposed in order to remedy and overcome the limitations of CCM. Sladek et al. [15] proposed a meshfree local BIEM in the dynamic fracture analysis of anti-plane crack on FGMs and further implemented it in the in-plane fracture analysis [16]. Dai et al. [17] employed the meshfree radial point interpolation method (X-RPIM) in the numerical simulations of FGM plate. Bui et al. [18] further utilized the X-RPIM along with the newly proposed meshfree Galerkin method based on moving kriging interpolation in the fracture analysis of FGM structure. By eliminating the correlation parameter effects, this method had shown good accuracy in the calculation of DSIF in FGMs. Thai et al. [19] utilized this method in the investigation of fracture behaviors of isotropic and sandwich FGM plate. Imachi et al. [20] utilised the OSPD in the evaluation of mixed-mode fracture analysis of 2D plate by employing the moving least-squares approximation. Dai et al. [21-24] studied the in-plane and out-of-plane fracture behaviors of shell structures by using OSPD. Furthermore, Ozdemir et al. [25] applied the OSPD in the simulation of dynamic wave propagation and crack propagation in FGM. Yang et al. [26] developed a peridynamic (PD) formulation for higher order beam with FGM by using Euler-Lagrange equation and Taylor's expansion. The proposed method was validated by several typical benchmark problems of beam and compared by FEM, which shows a good accuracy.

Though PD is a newly emerged meshfree method during the past decade, it is not fully exploited and understood in the fracture analysis of FGM. Therefore, in this article, in-depth studies about fracture behaviors on FGM by using OSPD is presented. Different from analytical and classic numerical analyses, the fracture characteristics will be evaluated in a meshfree and non-local perspective. Interaction integral by considering the material gradients are utilised in SIFs calculations. In FGM modeling, different material average schemes are introduced and the influence of these schemes on the accuracy of

numerical simulations is discussed. Meanwhile, PDDO is employed in transforming the physical derivatives into the corresponding spatial integration form, which will suit well with OSPD framework. Results are compared with the reference solutions provided in the literature. The paper is arranged as follows. In the second section, fundamental knowledge of OSPD and PDDO are introduced, and the formulations of interaction integral on FGM are provided in the third section. Then several numerical examples will be discussed in the fourth section. Finally, the proposed method and results will be briefly summarized in the last section.

2. Peridynamic theory

Initially introduced by Silling [27], PD, later named as BBPD, is regarded as an extension of solid mechanics. Structures or problem domains are uniformly discretized by finite number of material points with certain volume in this theory. Different from FEM, as a nonlocal theory, each material point can build up interactions with surrounding points within certain distance. The set of these points is called "horizon" (H_x) and the shape of horizon is, usually, a disc and a sphere for 2D and 3D modeling, respectively. The radius of the horizon is usually denoted as "δ". The size of the horizon may have some influence on numerical simulation [28-30], and when it shrinks to zero, the CCM formulation will be derived [31]. Horizon size is selected as three times of the grid space in consideration of accuracy and computing time. The interaction between each pair material points is named as "bond", and pairwise force may occur due to the deformation of bond. However, BBPD is oversimplified and it has many limitations in real applications. In BBPD, pairwise forces are equal in magnitude but opposite in direction. In this manner, there is a limitation on material properties, such as the Poisson's ratio has to be 1/3 in 2D and 1/4 in 3D analysis, respectively, for isotropic materials, which is not suitable for FGM fracture analysis. Hence, to overcome this limitation, Silling et al. [32] further optimized the theory and proposed OSPD by redefining material-dependent parameter and introducing the concept of "state".

2.1. Equation of motion

According to Silling et al. [32] and later Madenci and Oterkus [33], in OSPD, the motion of a material point $\boldsymbol{x}_i$ at time t can be numerically ex-

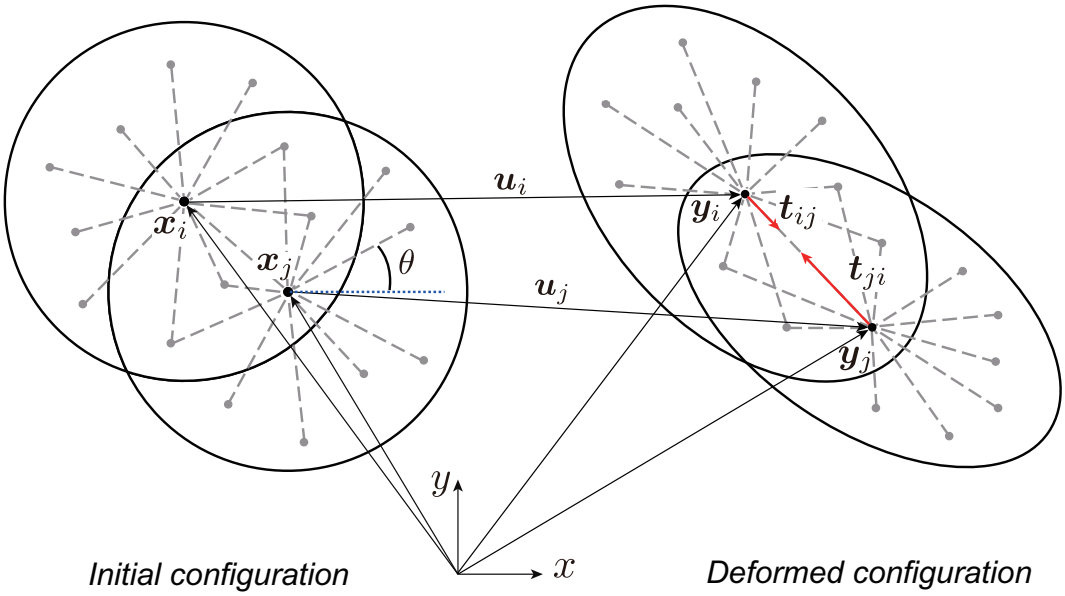

Figure 1: Horizon and pairwise force in OSPD.

pressed as:

$$\rho_i(\boldsymbol{x})\ddot{\boldsymbol{u}}_i(\boldsymbol{x}_i,t)=\sum_{j=1}^{n}[\boldsymbol{t}_{ij}(\boldsymbol{u}_i,\boldsymbol{u}_j,\boldsymbol{x}_i,\boldsymbol{x}_j,t)-\boldsymbol{t}_{ji}(\boldsymbol{u}_i,\boldsymbol{u}_j,\boldsymbol{x}_i,\boldsymbol{x}_j,t)]V_j+\boldsymbol{b}_i(t), \quad (1)$$

where $\rho_i(\boldsymbol{x})$ is the mass density of points i. $\boldsymbol{x}_i$ and $\boldsymbol{x}_j$ are initial position of points i and j, respectively. $\boldsymbol{u}_i$ and $\boldsymbol{u}_j$ are the displacement of points i and j, respectively. $\boldsymbol{t}_{ij}$ and $\boldsymbol{t}_{ji}$ are force states of points i and j, respectively. Even though $\boldsymbol{t}_{ij}$ has similar expression with $\boldsymbol{t}_{ji}$, they may not be the same since they are determined by material points within their own horizons, as shown in Fig. 1. V_j is the volume of material point j and $\boldsymbol{b}_i$ is body force density of material point i. The force state is derived from strain energy density, W_i, which is composed of dilatation and distortion terms for isotropic homogeneous material. For FGM, some special treatments on material properties are necessary, which are illustrated in detail in Section 2.4. Strain energy

density and force state can be numerically presented as:

$$W_i = a_1 \Theta_i^2 + b \sum_{j=1}^{n} \omega_{ij} \left(|\boldsymbol{y}_j - \boldsymbol{y}_i| - |\boldsymbol{x}_j - \boldsymbol{x}_i| \right)^2 V_j, \tag{2a}$$

$$\boldsymbol{t}_{ij} = \frac{1}{V_j} \frac{\partial W_i}{\partial \left(|\boldsymbol{y}_j - \boldsymbol{y}_i| \right)} \frac{\boldsymbol{y}_j - \boldsymbol{y}_i}{|\boldsymbol{y}_j - \boldsymbol{y}_i|}, \tag{2b}$$

where n is the number of material points in the horizon of material point i. ω_{ij} is the weight function which characterize the strength of the interaction between points i and j. $\boldsymbol{y}_i$ and $\boldsymbol{y}_j$ are new positions of points i and j, respectively, after deformation. For 2D problem, the dilatation term Θ_i can be expressed as:

$$\Theta_i = d \sum_{j=1}^{n} \omega_{ij} s_{ij} \frac{\boldsymbol{y}_j - \boldsymbol{y}_i}{|\boldsymbol{y}_j - \boldsymbol{y}_i|} \cdot (\boldsymbol{x}_j - \boldsymbol{x}_i) V_j. \tag{3}$$

The expression of weight function ω_{ij} and bond stretch, s_{ij}, can be shown as:

$$\omega_{ij} = \frac{\delta}{|\boldsymbol{x}_j - \boldsymbol{x}_i|}, \;\; s_{ij} = \frac{|\boldsymbol{y}_j - \boldsymbol{y}_i| - |\boldsymbol{x}_j - \boldsymbol{x}_i|}{|\boldsymbol{x}_j - \boldsymbol{x}_i|}. \tag{4}$$

PD parameters a_1, b and d, in Eq. (2a) and Eq. (3) can be expressed as:

$$a_1 = \frac{\lambda\alpha - \mu}{2}, \;\; b = \frac{6\mu}{\pi h \delta^4}, \;\; d = \frac{2}{\pi h \delta^3}, \tag{5}$$

where h is plate thickness. Lamé's constants, λ and μ, and coefficient α can be presented as:

$$\lambda = \frac{E\nu}{(1+\nu)(1-2\nu)}, \;\; \mu = \frac{E}{2(1+\nu)}, \tag{6a}$$

$$\alpha = \begin{cases} (1-2\nu)/(1-\nu) & \text{for plane stress} \\ 1 & \text{for plane strain} \end{cases}. \tag{6b}$$

2.2. Damage

Bond will either elongate or contract as the structure deforms under loading, and it will irreversibly break once bond stretch exceeds a critical value, s_c, as shown in Fig. 2. A coefficient $m(\boldsymbol{x}_i, \boldsymbol{x}_j, t)$ is applied to illustrate the situation of bond connection. For unbroken bond, $m(\boldsymbol{x}_i, \boldsymbol{x}_j, t)$ is equal to 1. For broken bond, $m(\boldsymbol{x}_i, \boldsymbol{x}_j, t)$ is equal to 0. Therefore, the damage of

material point, $\boldsymbol{x}_i$, is the percentage of broken bonds in its horizon, which can be numerically presented as:

$$\Phi(\boldsymbol{x}_i, t) = 1 - \frac{\int_{H_x} m(\boldsymbol{x}_i, \boldsymbol{x}_j, t) dV}{\int_{H_x} dV}. \tag{7}$$

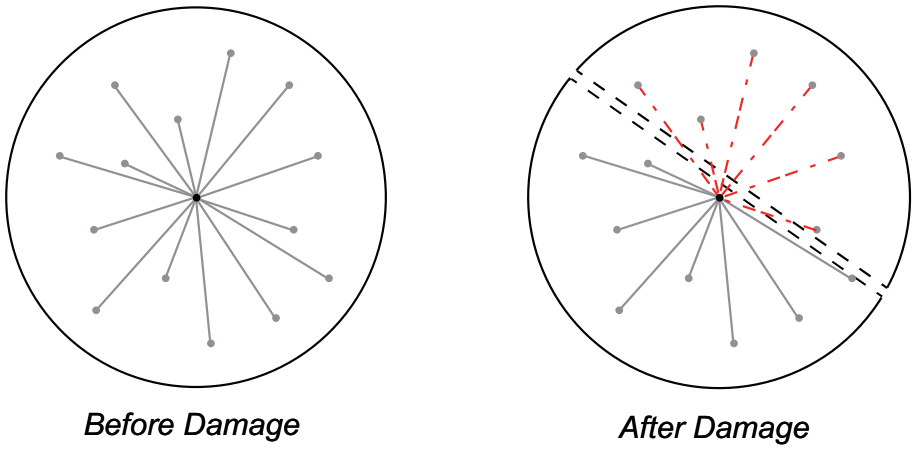

Figure 2: Damage evolution.

2.3. Peridynamic differential operator

PDEs, as a fundamental mathematical tool, have been frequently employed in the numerical modeling of various natural phenomena and engineering applications. Due to the complexity in specific problems, analytical methods might not always be utilized in solving the PDEs directly. Therefore, many numerical techniques, such as FEM [34], FDM [35] and BEM [36], have been developed in PDE approximation. However, the geometrical discontinuity and singularity in fracture analysis may bring mathematical difficulties for these methods. Therefore, based on the framework of PD, Madenci et al. [37] proposed the PDDO to approximate the PDEs in a nonlocal meshfree perspective. By using PDDO, the PDEs are reformulated by spatial integral equations, which overcome the problems induced by damages and failures. In this article, 2D formulations of PDDO will be illustrated.

PDDO is derived from the Taylor Series. The 2D second order Taylor Series can be expanded as:

$$\begin{aligned} f(\boldsymbol{x}_j) = f(\boldsymbol{x}_i) + \xi_1 \frac{\partial f(\boldsymbol{x}_i)}{\partial x} + \xi_2 \frac{\partial f(\boldsymbol{x}_i)}{\partial y} + \frac{1}{2!}\xi_1^2 \frac{\partial^2 f(\boldsymbol{x}_i)}{\partial x^2} \\ + \frac{1}{2!}\xi_2^2 \frac{\partial^2 f(\boldsymbol{x}_i)}{\partial y^2} + \xi_1\xi_2 \frac{\partial f(\boldsymbol{x}_i)}{\partial x \partial y} + R, \end{aligned} \tag{8}$$

where $f(\boldsymbol{x}_i)$ and $f(\boldsymbol{x}_j)$ are values of functions at material points i and j, respectively. ξ_1 and ξ_2 are components of initial bond length $\boldsymbol{\xi}$ ($\boldsymbol{\xi}$=$\boldsymbol{x}_j$-$\boldsymbol{x}_i$) in x- and y-directions, respectively. R represents the remainder terms, which is assumed small enough to be neglected in this research. Rearranging Eq. (8) by moving the first term on the right-hand side to the left-hand side and multiplying a 2D orthogonal PD function ($g_2^{p_1p_2}(\boldsymbol{\xi})$) for all the terms on both sides, and then integrating through the horizon yield as:

$$\begin{aligned} &\int_{H_x} (f(\boldsymbol{x}_j) - f(\boldsymbol{x}_i)) g_2^{p_1p_2}(\boldsymbol{\xi}) dV = \frac{\partial f(\boldsymbol{x}_i)}{\partial x} \int_{H_x} \xi_1 g_2^{p_1p_2}(\boldsymbol{\xi}) dV \\ &+ \frac{\partial f(\boldsymbol{x}_i)}{\partial y} \int_{H_x} \xi_2 g_2^{p_1p_2}(\boldsymbol{\xi}) dV + \frac{\partial^2 f(\boldsymbol{x}_i)}{\partial x^2} \int_{H_x} \frac{1}{2!}\xi_1^2 g_2^{p_1p_2}(\boldsymbol{\xi}) dV \\ &+ \frac{\partial^2 f(\boldsymbol{x}_i)}{\partial y^2} \int_{H_x} \frac{1}{2!}\xi_2^2 g_2^{p_1p_2}(\boldsymbol{\xi}) dV + \frac{\partial^2 f(\boldsymbol{x}_i)}{\partial x \partial y} \int_{H_x} \xi_1\xi_2 g_2^{p_1p_2}(\boldsymbol{\xi}) dV, \end{aligned} \tag{9}$$

where p_1, p_2=0, 1, 2 except p_1=p_2=0. Recalling the orthogonal property of PD function:

$$\frac{1}{n_1!n_2!} \int_{H_x} \xi_1^{n_1}\xi_2^{n_2} g_2^{p_1p_2}(\boldsymbol{\xi}) dV = \delta_{n_1p_1}\delta_{n_2p_2} \quad \text{with} \quad n_1, n_2 = 0, 1, 2, \tag{10}$$

where δ_{np} is Kronecker delta. Substituting Eq. (10) into Eq. (9), the relationship between PDEs and integral equation can be established correspondingly within the PD framework as:

$$\begin{Bmatrix} \frac{\partial f(\boldsymbol{x}_i)}{\partial x} \\ \frac{\partial f(\boldsymbol{x}_i)}{\partial y} \\ \frac{\partial^2 f(\boldsymbol{x}_i)}{\partial x^2} \\ \frac{\partial^2 f(\boldsymbol{x}_i)}{\partial y^2} \\ \frac{\partial^2 f(\boldsymbol{x}_i)}{\partial x \partial y} \end{Bmatrix} = \int_{H_x} (f(\boldsymbol{x}_j) - f(\boldsymbol{x}_i)) \begin{Bmatrix} g_2^{10}(\boldsymbol{\xi}) \\ g_2^{01}(\boldsymbol{\xi}) \\ g_2^{20}(\boldsymbol{\xi}) \\ g_2^{02}(\boldsymbol{\xi}) \\ g_2^{11}(\boldsymbol{\xi}) \end{Bmatrix} dV. \tag{11}$$

The PD functions are determined by the numerical configuration in PD framework and detailed calculation processes of PD functions can be found in many researches in the literature, such as [38,39]. For 2D analysis, the PD functions can be expressed as:

$$g_2^{10}(\boldsymbol{\xi}) = \frac{2}{\pi h|\boldsymbol{\xi}|\delta^2}\cos\theta, \tag{12a}$$

$$g_2^{01}(\boldsymbol{\xi}) = \frac{2}{\pi h|\boldsymbol{\xi}|\delta^2}\sin\theta, \tag{12b}$$

$$g_2^{20}(\boldsymbol{\xi}) = \frac{9}{\pi h|\boldsymbol{\xi}|\delta^3}\cos^2\theta - \frac{3}{\pi h|\boldsymbol{\xi}|\delta^3}\sin^2\theta, \tag{12c}$$

$$g_2^{02}(\boldsymbol{\xi}) = -\frac{3}{\pi h|\boldsymbol{\xi}|\delta^3}\cos^2\theta + \frac{9}{\pi h|\boldsymbol{\xi}|\delta^3}\sin^2\theta, \tag{12d}$$

$$g_2^{11}(\boldsymbol{\xi}) = \frac{12}{\pi h|\boldsymbol{\xi}|\delta^3}\cos\theta\sin\theta, \tag{12e}$$

where θ refers to the angle between bond and horizontal axis in initial configuration in Cartesian coordinate system as shown in Fig. 1. Substituting Eq. (12) to Eq. (11), the 2D PDEs can be approximated. The expression of 1D and 3D PD functions can be found in [40] and previous researches [41,42].

2.4. FGM modeling

Equations in Section 2.1 are only valid for homogeneous isotropic materials. For FGMs, extreme refined discretization scheme might be of vital importance. In this way, the difference of material properties between material points within the horizon is small, which can be regarded as homogeneous materials. Otherwise, it might cause errors if they are directly utilized. Therefore, modifications on these equations are necessary.

Average schemes for material properties are commonly used in the literature in dealing with the nonhomogeneous problems. By assuming the structures as the homogeneous material locally, the averaged material properties of each bond can be derived from those of the pairwise points associated with this bond. Ozdemir et al. [25] calculated direct average for material properties of bonds in evaluating the crack propagation in structures with FGM. Rahimi et al. [43] investigated the relationships of the material properties among the points within the horizon, and proposed an arithmetic average scheme by defining a coefficient, named dominancy rate. They found out

it has a better accuracy in crack propagation prediction as compared with traditional PD. Similar average schemes can be found in [44] and [45]. On the other hand, Behera et al. [46] utilized a Heaviside function in bi-material analysis by using non-ordinary state based PD. The material properties are respectively assigned to the material points on bond, instead of taking the average value. Nguyen et al. [47] applied a harmonic average scheme in the researches of bi-material by using OSPD. Inspired by their approaches, the harmonic average scheme is also introduced to the numerical simulation. The direct average scheme, arithmetic average scheme and harmonic average scheme can be expressed, respectively, as:

$$P_{\text{avg}} = \frac{P_i + P_j}{2}, \tag{13a}$$

$$P_{\text{avg}} = \frac{\omega_f \times \min(P_i, P_j) + \max(P_i, P_j)}{\omega_f + 1}, \tag{13b}$$

$$P_{\text{avg}} = \frac{\omega_f + 1}{\frac{\omega_f}{\min(P_i,P_j)} + \frac{1}{\max(P_i,P_j)}}, \tag{13c}$$

where P_{avg} refers to the averaged material properties of the bond as shown in Fig. 3. ω_f is the weight coefficient in defining the average material properties on bond. P_i and P_j are material properties of pairwise points i and j respectively. The influence of these average schemes will be discussed in the Section 4.

3. Calculation of stress intensity factors in FGMs

SIF, as an important parameter in fracture analysis, is usually employed in describing the stress concentration at the vicinity of crack tips. For homogeneous materials, energy methods, such as J-integral method, are frequently applied in the evaluation of SIFs and DSIFs [10,11,48-51]. For FGM, Chen et al. [52] adopted the element-free Galerkin method (EFGM) in the calculation and evaluation of SIFs. They pointed out that the path independency, by using conventional J-integral method, might not always be accomplished in FGMs. Therefore, it is necessary to make modifications for J-integral formulations by considering the material gradient variation effects. In this article, J-integral method [10] is applied and the formulation of J-integral is shown as:

$$J = \lim_{\Gamma_0 \to 0} \int_{\Gamma_0} (W_i \delta_{1j} - \sigma_{ij} u_{i,1}) n'_j d\Gamma, \tag{14}$$

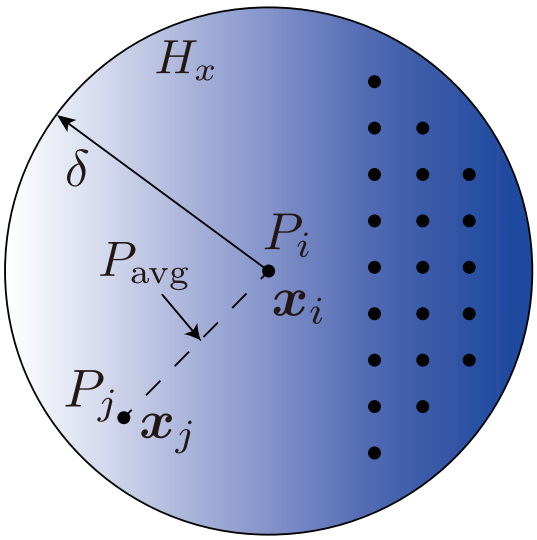

Figure 3: Diagram of material average scheme for a bond.

where $u_{i,1}$ with i=1, 2 refers to the partial derivatives of the displacements over x-coordinate under local coordinate system. Eq. (14) is the J-integral formulation in a contour form, where σ_{ij} is the Cauchy's stress component and n'_j refers to the unit normal vector to the contour as shown in Fig. 4(a). x' and y' are axes of local coordinate system located at the crack tip. However, since the line integral is not convenient in numerical simulations, it is transformed into domain integral based on equivalent domain integral [53], which can be expressed as:

$$J = \int_A (\sigma_{ij} u_{i,1} - W_i \delta_{1j}) q_{,j} dA + \int_A (\sigma_{ij} u_{i,1} - W_i \delta_{1j})_{,j} q dA, \tag{15}$$

where A is the area enclosed by Γ_0, Γ and crack surface. q is a manually defined weight function in the domain J-integral method. Frustum shape q-function is selected in the numerical simulations. On the contour edges, q is equal to 0. Within the region A_0, q is equal to unity. q linearly varies from 0 to 1 within the region A. The layout of q-function is illustrated by Fig. 4(b) and the expression of q-function can be written as:

$$q(x', y') = \begin{cases} 1 & \text{within } A_0 \\ (0, 1) & \text{within } A \\ 0 & \text{outside } A \end{cases}. \tag{16}$$

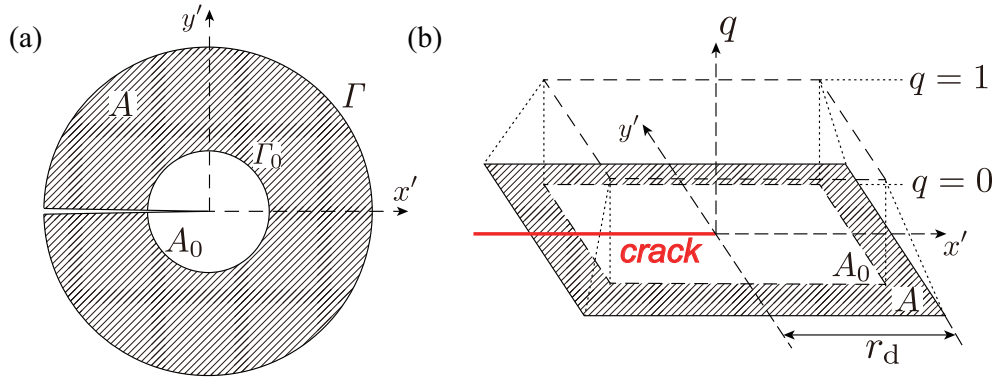

Figure 4: Layouts of J-integral: (a) J-integral contour, (b) Distribution of q-function.

By superimposing the actual and auxiliary fields (denoted as superscript, aux) of Eq. (15), the interaction integral formulation can be derived. The superimposing J-integral formulation, J^{sup}, is given as:

$$\begin{aligned} J^{\mathrm{sup}} = &\int_A [(\sigma_{ij} + \sigma_{ij}^{\mathrm{aux}})(u_{i,1} + u_{i,1}^{\mathrm{aux}}) - (W_i + W_i^{\mathrm{aux}})\delta_{1j}]q_{,j}dA \\ &+ \int_A [(\sigma_{ij} + \sigma_{ij}^{\mathrm{aux}})(u_{i,1} + u_{i,1}^{\mathrm{aux}}) - (W_i + W_i^{\mathrm{aux}})\delta_{1j}]_{,j}qdA. \end{aligned} \tag{17}$$

By decomposing Eq. (17), the interaction integral (M-integral) can be derived by actual field J and auxiliary field J^{aux} as:

$$M = J^{\mathrm{sup}} - J - J^{\mathrm{aux}}, \tag{18a}$$

$$\begin{aligned} M = &\int_A [(\sigma_{ij}^{\mathrm{aux}} u_{i,1} + \sigma_{ij} u_{i,1}^{\mathrm{aux}}) - \sigma_{ik}^{\mathrm{aux}} \varepsilon_{ik} \delta_{1j}]q_{,j}dA \\ &+ \int_A (-C_{ijkl,1}\varepsilon_{kl}^{\mathrm{aux}}\varepsilon_{ij} + \sigma_{ij,j}^{\mathrm{aux}} u_{i,1} + \rho\ddot{u}_i u_{i,1}^{\mathrm{aux}})qdA, \end{aligned} \tag{18b}$$

where ε_{ij} is elastic strain component and C_{ijkl} is the constitutive tensor. The auxiliary elastic strains are derived from displacement components, which can be expressed as:

$$u_i^{\mathrm{aux}} = K_{\mathrm{I}}^{\mathrm{aux}} l_{\mathrm{I}}(r, \phi) + K_{\mathrm{II}}^{\mathrm{aux}} l_{\mathrm{II}}(r, \phi), \tag{19}$$

where r represents the distance to the crack tip and ϕ refers to the inclined angle with respect to the horizontal axis in local coordinate system as shown in Fig. 5. $K_{\mathrm{I}}^{\mathrm{aux}}$ and $K_{\mathrm{II}}^{\mathrm{aux}}$ are mode-I and -II SIFs, respectively. Since the dynamic asymptotic fields for non-homogeneous materials has the similar

behaviour to that for quasi-static homogeneous materials [10], the asymptotic fields of Williams' solutions [54] are selected as the auxiliary fields in the FGM structure. The expression of l_{I} and l_{II} can be found in literature, such as [55].

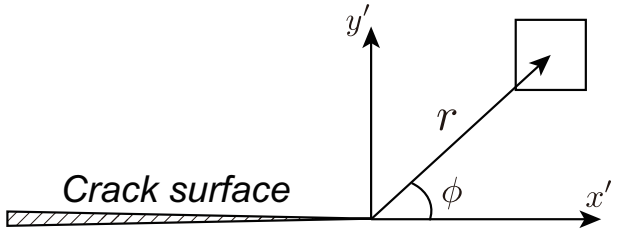

Figure 5: Local coordinate system originated at the crack tip for auxiliary field.

According to [10], in non-homogeneous materials, equilibrium conditions are not satisfied, and thus, the auxiliary stress components have to follow the non-homogeneous constitutive relations. Therefore, the auxiliary strain field and corresponding stress field can be expressed as:

$$\varepsilon_{ij}^{\mathrm{aux}} = \frac{1}{2}(u_{i,j}^{\mathrm{aux}} + u_{j,i}^{\mathrm{aux}}), \tag{20a}$$

$$\sigma_{ij}^{\mathrm{aux}} = C_{ijkl}\varepsilon_{ij}^{\mathrm{aux}}, \tag{20b}$$

where C_{ijkl} is the spatially varied constitutive tensor. For a better understanding of SIF in FGM, Eq. (18b) can be decomposed by six terms as:

$$\text{Term 1} = \int_A \sigma_{ij}^{\mathrm{aux}} u_{i,1} q_{,j} dA, \tag{21a}$$

$$\text{Term 2} = \int_A \sigma_{ij} u_{i,1}^{\mathrm{aux}} q_{,j} dA, \tag{21b}$$

$$\text{Term 3} = -\int_A \sigma_{ik}^{\mathrm{aux}} \varepsilon_{ik} \delta_{1j} q_{,j} dA, \tag{21c}$$

$$\text{Term 4} = -\int_A C_{ijkl,1} \varepsilon_{kl}^{\mathrm{aux}} \varepsilon_{ij} q dA, \tag{21d}$$

$$\text{Term 5} = \int_A \sigma_{ij,j}^{\mathrm{aux}} u_{i,1} q dA, \tag{21e}$$

$$\text{Term 6} = \int_A \rho \ddot{u}_i u_{i,1}^{\mathrm{aux}} q dA. \tag{21f}$$

In Eqs. (21a)-(21f), Terms 1, 2 and 3 refer to the static effects and material homogeneity, while Terms 4 and 5 represent the material non-homogeneity. Term 6 shows the dynamic effect of the interaction integral. For static and homogeneous fracture analysis, Terms 4, 5 and 6 are equal to zero. The partial derivatives in Eqs. (21a)-(21f) can be transformed into spatial integral equations by using PDDO, which can be expressed as:

$$u_{i,1} = \int_{H_x} (u_i' - u_i) g_2^{10}(\boldsymbol{\xi}) dV, \tag{22a}$$

$$u_{i,1}^{\text{aux}} = \int_{H_x} ((u_i^{\text{aux}})' - u_i^{\text{aux}}) g_2^{10}(\boldsymbol{\xi}) dV, \tag{22b}$$

$$C_{ijkl,1} = \int_{H_x} (C_{ijkl}' - C_{ijkl}) g_2^{10}(\boldsymbol{\xi}) dV, \tag{22c}$$

$$\sigma_{ij,1}^{\text{aux}} = \int_{H_x} ((\sigma_{ij}^{\text{aux}})' - \sigma_{ij}^{\text{aux}}) g_2^{10}(\boldsymbol{\xi}) dV, \tag{22d}$$

$$\sigma_{ij,2}^{\text{aux}} = \int_{H_x} ((\sigma_{ij}^{\text{aux}})' - \sigma_{ij}^{\text{aux}}) g_2^{01}(\boldsymbol{\xi}) dV, \tag{22e}$$

$$q_{,1} = \int_{H_x} (q' - q) g_2^{10}(\boldsymbol{\xi}) dV, \tag{22f}$$

$$q_{,2} = \int_{H_x} (q' - q) g_2^{01}(\boldsymbol{\xi}) dV, \tag{22g}$$

where u_i with i=1, 2 represents the displacement component along x- or y-coordinate. The superscript "$\prime$" in Eqs. (22a)-(22g) refers to the corresponding value on the neighbour points within horizon. The contribution of each term on the evaluation of SIFs and DSIFs will be demonstrated in the following numerical studies.

4. Numerical examples

Several standard benchmark problems will be evaluated and discussed for a better understanding of FGM fracture behaviors. In Section 4.1, static fracture analysis on edge-cracked strip is presented. Meanwhile, the influence of different material average schemes in FGM modeling on fracture analysis is also compared. In Section 4.2, a central-cracked plate under tensile loading is considered. The static mode-I SIF of FGM is also under investigation.

In Sections 4.3, 4.4 and 4.5, dynamic fracture analyses on central cracked structures with different material variation are conducted. DSIFs of these cases are numerically evaluated respectively.

For a better understanding of SIFs and DSIFs, the normalized solutions are provided in these numerical simulations, which are given as:

$$K_i^* = \frac{K_i}{\sigma_t(x)\sqrt{\pi a}} \ (i = \mathrm{I}, \mathrm{II}), \tag{23}$$

where $\sigma_t(x)$ refer to the applied tensile loading. For static analysis, one of the solutions is equating the $\rho_i(\boldsymbol{x})\ddot{\boldsymbol{u}}_i(\boldsymbol{x}_i, t)$ in Eq. (1) to zero. By reformulating the loading matrix and stiffness matrix, the displacement field in static state can be derived. However, an excellent computing performance is required in matrix calculation, especially for problems with refined discretization, complex geometries and sophisticated loading conditions. As an alternative option, adaptive dynamic relaxation (ADR) method is introduced into PD by Kilic and Madenci [56]. In ADR, a manually defined damping factor is introduced into dynamic motion, which lead to a fast convergence of solution. In this way, the static solutions can be derived by the dynamic formulation and it is not sensitive to the time step size by employing the explicit time integration. In the following simulations, ADR is utilized in the static fracture analysis.

4.1. Edge-cracked strip under tensile loading

Fig. 6 shows a 2D strip with a crack of length, a. The strip is free of constrain and uniform tensile loading, $\sigma_t(x)$, is applied on the left and right edges. The length and width of the strip is 1.0 m and 8.0 m, respectively. The ratio of crack length on strip length varies from 0.4 to 0.6. Poisson's ratio remains to be 0.25. Elastic modulus function, $E(x)$, varies along the x-axis, and the ratio between elastic modulus on upper and lower edges, E_2/E_1, is equal to 10. The exponential relation can be presented as:

$$E(x) = E_1 e^{\beta_1 x}, \ \beta_1 = \frac{\ln(E_2/E_1)}{Width}, \tag{24}$$

where E_1 and E_2 are elastic modulus on upper and lower edges, respectively. Coarse (Δx=0.02 m), intermediate (Δx=0.01 m) and refined (Δx=0.005 m) discretization schemes are uniformly defined in OSPD framework. Plane strain assumption is applied.

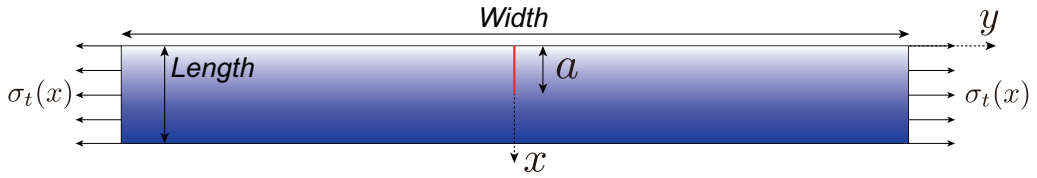

Figure 6: Edge-cracked strip under tensile loading.

Fig. 7 shows the comparisons between four treatments of material properties on bond in different discretization schemes. The weighted coefficient in Eq. (13b) and Eq. (13c) are selected as 100 based on [25]. Fig. 7(a) shows comparison of the crack opening displacement between FEM solution and OSPD solutions for coarse discretization. Results have reached good agreements with each other. The difference between OSPD solutions and analytical solutions by [5] with respect to normalized mode-I SIF is shown as Fig. 7(b). As the grid spacing is decreasing, the OSPD solutions converged to the reference solutions. For refined discretization scheme, the differences can remain within 0.2%. The results provided by these average scheme do not show obvious difference in the static mode-I SIF evaluations. The Heaviside and direct average schemes exhibit slightly higher accuracy in coarse and intermediate discretizations, while the differences among these schemes diminish in refined discretization due to the local homogenization of material properties. The mode-I SIF calculated by OSPD with harmonic average scheme has relatively large error (0.17%) as compared with other schemes in refined discretization. By considering the accuracy of numerical simulations, the refined discretization scheme is employed for the fracture analysis based on current OSPD formulations.

For problems with material discontinuity, such as inclusion or layered structure, there might be differences in displacement fields and SIFs calculation by using different average schemes in material properties [25]. Since FGM is continuously varied, the material discontinuity does not exist in the structure or solution domain. Difference average schemes might not have obvious influence on numerical solutions. Therefore, the selection of the material average scheme in FGM modeling can be relatively arbitrary in refined discretization. Hence, the Heavisde scheme is utilised in all numerical cases.

Table 1 shows the OSPD solutions, analytical solutions [5], FEM solutions [12] and EFGM solutions [52] in the mode-I SIF evaluations of the

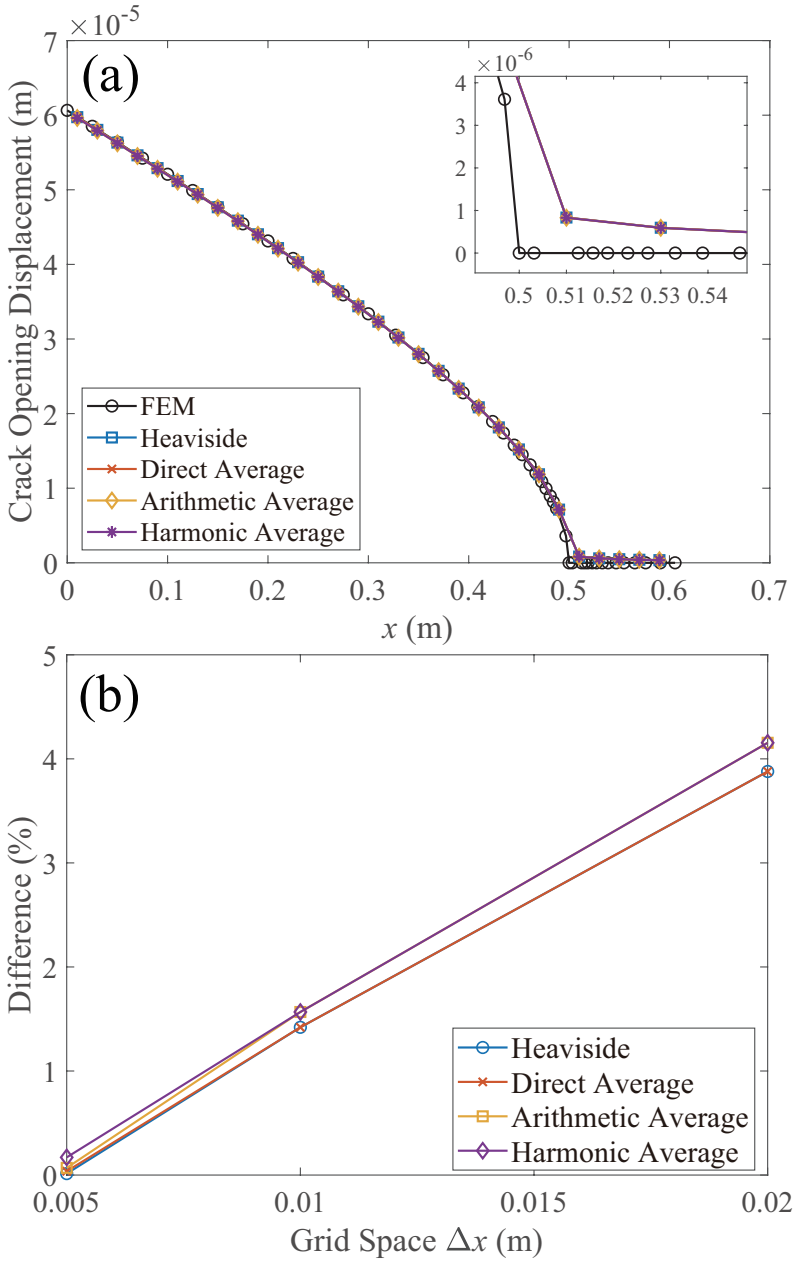

Figure 7: Convergence study of material average schemes: (a) Crack opening displacement, (b) Difference with respect to reference solution in terms of SIF.

Table 1: Comparison of K_{I}^{*} between OSPD and reference solutions for edge-cracked strip.

$a/Length$	r_{d}	K_{I}^{*}	K_{I}^{*} [5]	K_{I}^{*} [12]	K_{I}^{*} [52]
0.4	$30\Delta x$	1.5787	1.588	1.582	1.615
	$50\Delta x$	1.5767			
	$70\Delta x$	1.5765			
0.5	$30\Delta x$	2.1751	2.176	2.174	2.223
	$50\Delta x$	2.1763			
	$70\Delta x$	2.1794			
0.6	$30\Delta x$	3.2267	3.212	3.207	3.337
	$50\Delta x$	3.2349			
	$70\Delta x$	3.2319			

edge-cracked strip. Due to the symmetric loading and boundary conditions, half plate model was established by 617 nodes in FEM. In EFGM, full plate model was defined with 2,855 nodes. In order to maintain the accuracy, 200×1,600 material points are set up for the full plate model in OSPD. K_{I}^{*} is the normalized mode-I SIF. For different contour size, r_{d}, as shown in Fig. 4(b), the OSPD solutions remain stable which restore the path independency of interaction integral. Meanwhile, the difference between OSPD solutions and the reference solutions from [5,12] is below 1% for all crack length scenario, while there are relatively large differences with respect to the EFGM solutions provided by Chen et al. [52]. As the crack length increases, the K_{I}^{*} also rises due to the increase of stain energy release rate. The comparison has shown the good accuracy of the OSPD in mode-I SIF calculation.

4.2. Central-cracked plate under tensile loading

A 2D squared plate with horizontally oriented crack located in central region is selected as the model in this case study, as shown in Fig. 8. Both of the plate length and width are 20 m and crack to length ratio ($2a/Length$) is defined as 0.1. Poisson's ratio is fixed as 1/3. The bottom edge is constrained in vertical direction, while an exponential tensile loading is subjected on the top edge. The left and right edges are free of constrain. The variation of elastic modulus and tensile loading on the plate can be expressed as:

$$E(x) = E_0 e^{\beta_1 x},\ \sigma_t(x) = \sigma_0 e^{\beta_1 x}, \tag{25}$$

where E_0 and σ_0 are elastic modulus and tensile loading on x=0, respectively. β_1 is the coefficient of material gradient. Two material gradients, $\beta_1 a$ equals

0.25 and 0.5, are investigated, respectively. The plate is uniformly discretized by 400×400 (Δx=0.05 m) material points. Results will be validated by reference solutions from [12,57]. Plane stress assumption is applied in this case study. Due to the variation of elastic modulus and tensile loading as shown in Eq. (24), uniform strain field can be derived for undamaged case. For central-crack case, it will lead to a pure mode-I crack scenario.

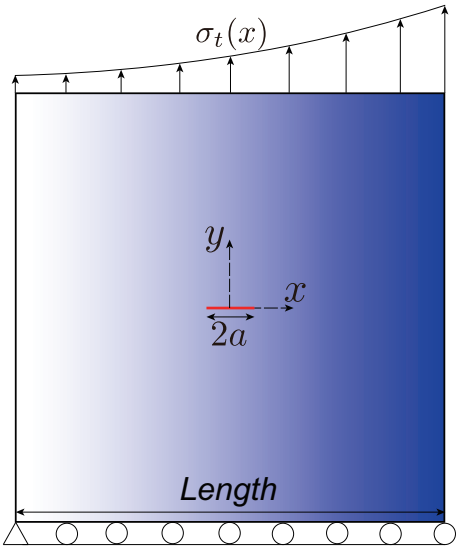

Figure 8: FGM plate with central crack under exponential tensile loading.

Table 2: Comparison of K_{I}^* between OSPD and reference solutions for central cracked plate.

$\beta_1 a$	r_{d}	$K_{\mathrm{I}}^*(a)$	$K_{\mathrm{I}}^*(-a)$	$\beta_1 a$	r_{d}	$K_{\mathrm{I}}^*(a)$	$K_{\mathrm{I}}^*(-a)$
	$12\Delta x$	1.2097	0.8252		$12\Delta x$	1.4418	0.6679
	$15\Delta x$	1.2107	0.8240		$15\Delta x$	1.4443	0.6662
0.25	$18\Delta x$	1.2101	0.8219	0.5	$18\Delta x$	1.4446	0.6639
	[12]	1.221	0.827		[12]	1.458	0.664
	[57]	1.196	0.825		[57]	1.424	0.674

Table 2 shows comparisons of OSPD solutions and reference solutions provided by [12] and [57] for the central cracked plate. $K_{\mathrm{I}}^*(a)$ and $K_{\mathrm{I}}^*(-a)$ represent the normalized mode-I SIFs on right and left crack tip regions, respectively. In general, the value of K_{I}^* at the left tip region is smaller than

that at the right tip region due to the difference in elastic modulus. As the material gradient increases, difference between left and right crack tips in terms of mode-I SIF becomes larger. Results between OSPD solutions are in good agreement with the references solution provided by [12], whose differences could be remained within 1%. Meanwhile, the path independency of the mode-I SIFs is also accomplished, which matches with the characteristic of interaction integral. Therefore, the accuracy and reliability of OSPD in mode-I fracture analysis are validated.

4.3. Vertically graded central-cracked strip under tensile loading

A rectangular structure with 20 mm in length, 40 mm in width and 4.8 mm in crack length is selected, which is shown in Fig. 9. The variation of material properties follows the relationships given follow:

$$E(x) = E_0 e^{(\beta_1 x + \beta_2 y)},\ \rho(x) = \rho_0 e^{(\beta_1 x + \beta_2 y)}, \tag{26}$$

where E_0, ρ_0 and ν are 199.992 GPa, 5,000 kg/m^3 and 0.3, respectively. Apart from uniform tensile loading, $\sigma_t(x)$, applied on top and bottom edges, the plate is free from constrain. Since the material is vertically graded, then the coefficient β_1 is equal to 0. Therefore, material properties on the left and right crack tip regions are the same. Hence, only right crack tip region is considered in this evaluation. Meanwhile, different β_2 values, 0, 0.05 and 0.1, are discussed in this section. Plane strain assumption is applied. The computing time t is normalized as:

$$t^* = C_\mathrm{d} \times \frac{t}{(0.5 \times Width)}, \tag{27}$$

where C_d is longitudinal wave speed. Based on [10], it can be expressed as:

$$C_\mathrm{d} = \sqrt{\frac{E_0(1-\nu)}{\rho_0(1+\nu)(1-2\nu)}}. \tag{28}$$

According to Eqs. (21), the influence of each term on the mode-I DSIF is shown in Figs. 10. For the case with β_2=0, a homogeneous plate is restored. Therefore, the influence of nonhomogeneous terms, Term 4 and Term 5, should theoretically vanish. However, due to the numerical errors occur in the approximation of PDEs, Term 5 might have minor values. By refining

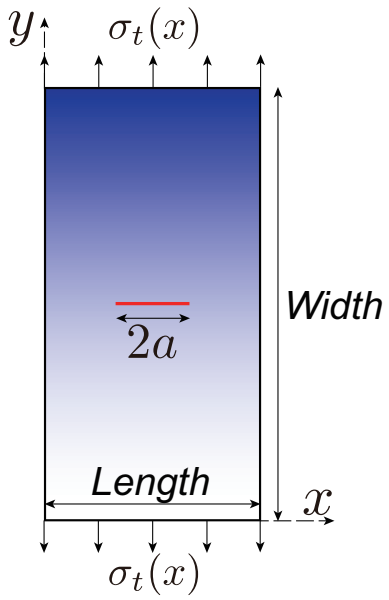

Figure 9: Vertically graded FGM plate under tensile loading.

the numerical model, this value will approach to 0. For nonhomogeneous material, due to the material of the plate is vertically graded, Term 4 remains zero based on Eq. (21d). As the β_2 increases, the influence of static terms increases around the first peak, while decreases faster after the second peak as shown in Fig. 10. The overall magnitude of static terms is larger than nonhomogeneous terms and the dynamic term, while the changes of nonhomogeneous terms are not noticeable as the variation of material gradients. The OSPD solution of mode-I DISF is also compared with the FEM solutions by Song and Paulino [10], as shown in Fig. 11. For all of the material gradients, good agreements between OSPD and FEM solutions can be observed, which prove the accuracy of OSPD in dynamic mode-I fracture analysis.

4.4. Horizontally graded slant cracked plate under tensile loading

A rectangular plate with a centrally located inclined crack is under investigation. As shown in Fig. 12, the length and width of the plate are 30 mm and 60 mm, respectively. Moreover, the crack is 14.14 mm in length with 45° inclined angle with respect to horizontal axis. Uniform tensile loading, $\sigma_t(x)$, is applied on top and bottom edges, while the left and right edges are free of constrain. The variation of material gradient follows the same

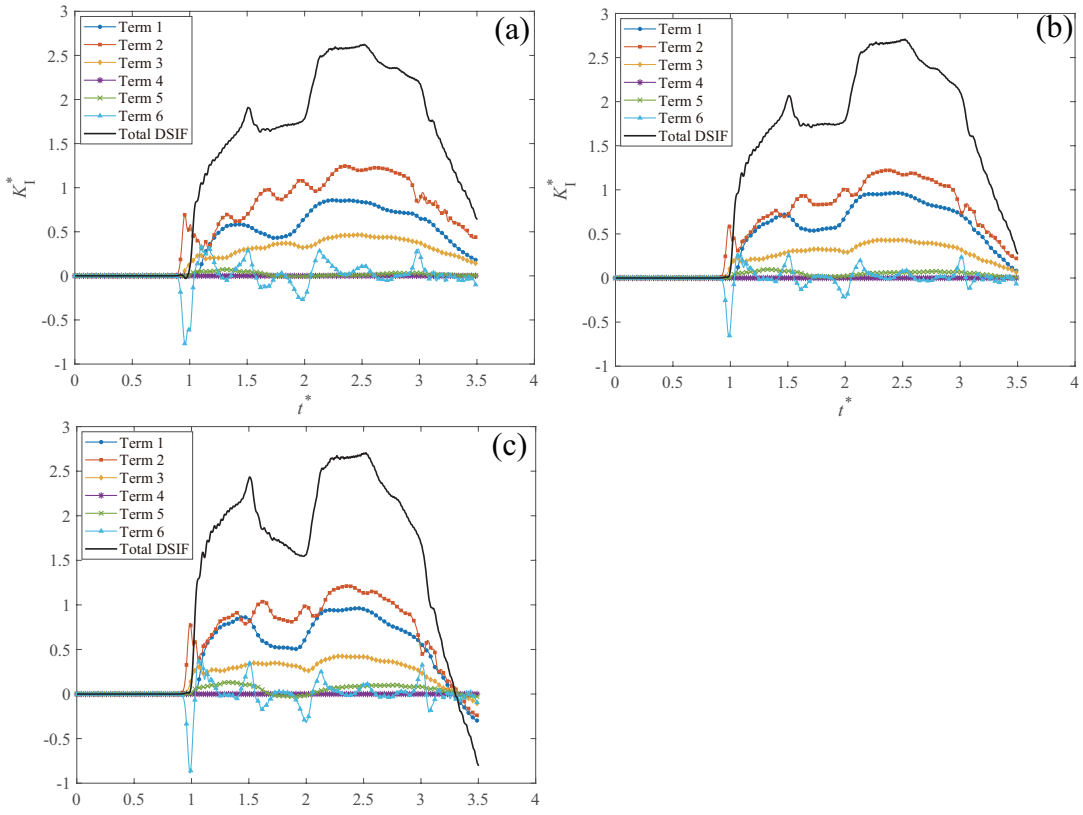

Figure 10: Contribution of each term on total DSIF:(a) β_2=0, (b) β_2=0.05, (c) β_2=0.1.

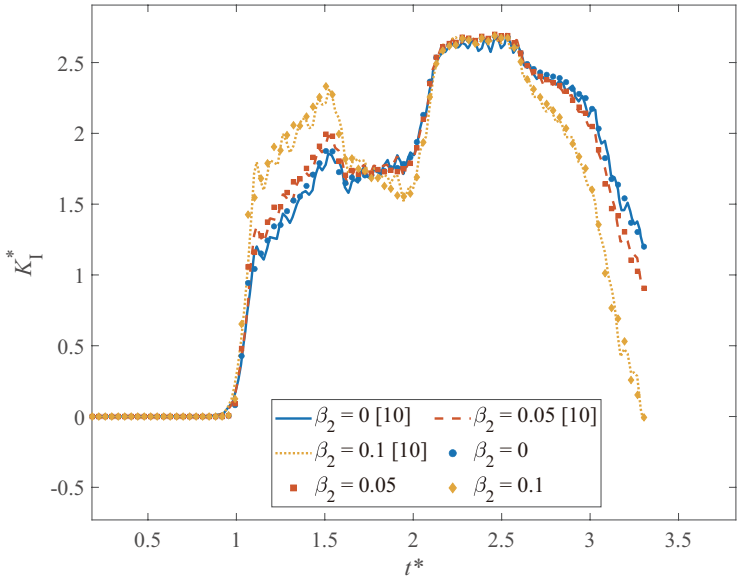

Figure 11: Comparison between OSPD and FEM on DSIF for β_1=0.

relationships as shown in Eq. (26). Since the material is horizontally graded, then β_2 is fixed as 0. Different material gradients, β_1=0, 0.05, 0.1 and 0.15, are tested and evaluated. Due to horizontally graded material, the material properties on the left and right crack tip regions are different. Therefore, the evolutions of mode-I DSIF over time at both left and right crack tip regions are discussed. Plane strain assumption is applied.

Fig. 13 shows the variation of mode-I DSIF at both left and right crack tip regions. As the material gradient, β_1, increase, the DSIFs at the right crack tip region increase. For the left crack tip region, the DSIFs decrease as the β_1 increases until around 15 μs, after which the variation of DSIFs changes. The DSIF solutions obtained by OSPD are also compared with FEM solutions [10]. Agreements in mode-I DSIF calculation can be observed from Fig. 13, which proves the reliability of OSPD in mode-I DSIF evaluation of FGMs.

4.5. Horizontally graded plate with hole under tensile loading

In this section, a rectangular plate with circular hole is presented in Fig. 14. Cracks with 30° inclined angle rise from the hole. The length and width of the plate are 30 mm and 60 mm, respectively. The distance between two

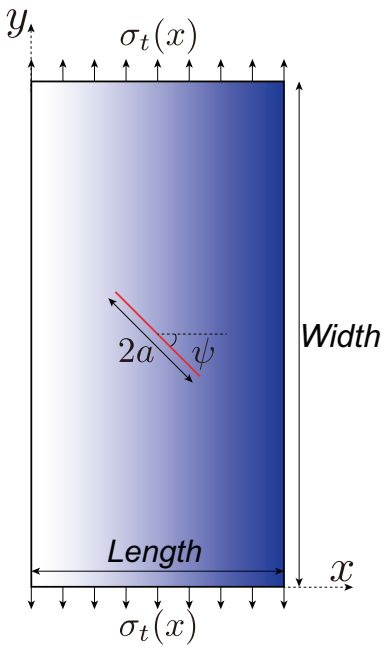

Figure 12: Slant cracked plate under tensile loading.

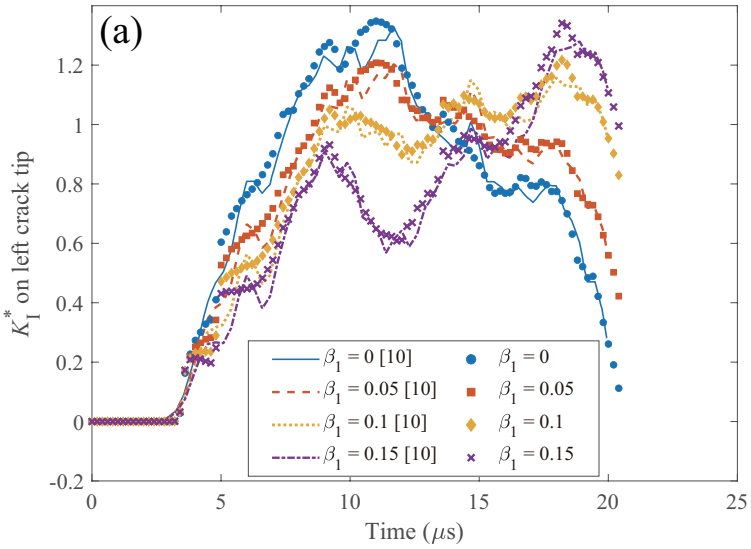

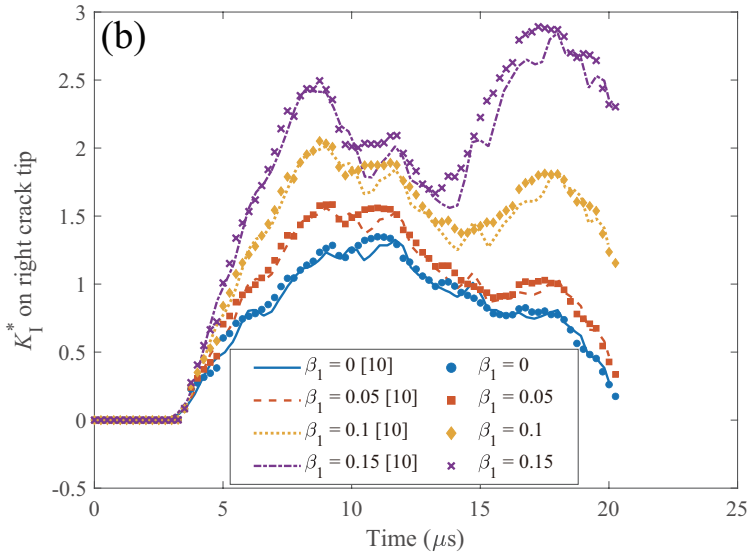

Figure 13: Comparison between OSPD solutions and reference solutions: (a) K_{I}^* at left crack tip region, (b) K_{I}^* at right crack tip.

crack tips is 15 mm and the radius of the hole, r', is 3.75 mm. Uniform tensile loading, $\sigma_t(x)$, is applied on the top and bottom edges, while the left and right edges are free of constrain. Poisson's ratio, ν, is fixed as 0.3. Plane strain assumption is applied. Material of the plate is horizontally varied, which can be expressed as:

$$E(x) = 224x + 7471 \ \ (\mathrm{MPa}), \tag{29a}$$

$$\rho(x) = 28.8x + 1380 \ \ (\mathrm{kg/m^3}). \tag{29b}$$

Fig. 15 shows the comparisons between OSPD solutions and FEM solutions [10] in terms of mixed-mode DSIFs. Generally, the absolute value of mode-I DSIF is larger than that of mode-II DISF due to the mode-I dominated situation in this case study. The magnitude of DSIF at the right crack tip region is larger than that at the left crack tip region, since the material properties at the right region is larger than that at the left region. Meanwhile, the DSIF initiation time at the left experiences slight delay as compared with that at the right. This is because the difference of longitudinal wave speed between left and right crack tip regions. By comparing

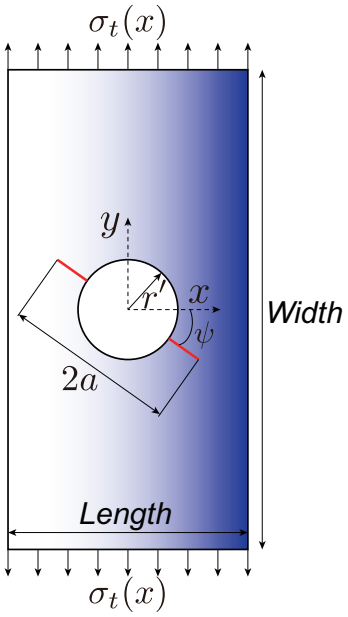

Figure 14: FGM plate with hole under tensile loading.

with the FEM solutions, OSPD has shown good accuracy in mode-I DSIF calculation. However, for mode-II DSIF evaluation, the accuracy is relatively low as compared with mode-I analysis due to the limitation of current OSPD formulation in capturing the shear deformation of structure.

5. Conclusion

In this study, a meshfree and nonlocal method, OSPD, is applied in the fracture analysis of FGM structures. OSPD has employed spatial integral equations in describing motion of structures, which avoids the limitation caused by geometric singularity in fracture analysis. Interaction integral methods by considering the material gradients of FGM is applied in the evaluation of SIFs and DSIFs. Meanwhile, PDDO is utilized to convert the local PDEs into nonlocal integral equations within the framework of PD.

Several numerical cases are implemented by using OSPD. First, the static behaviors of FGM plate with edged and central cracks are simulated, respectively. Different FGM modeling schemes and different discretization schemes are tested. For current OSPD formulation, the refined discretization scheme is necessary to maintain high accurate calculation. However, without con-

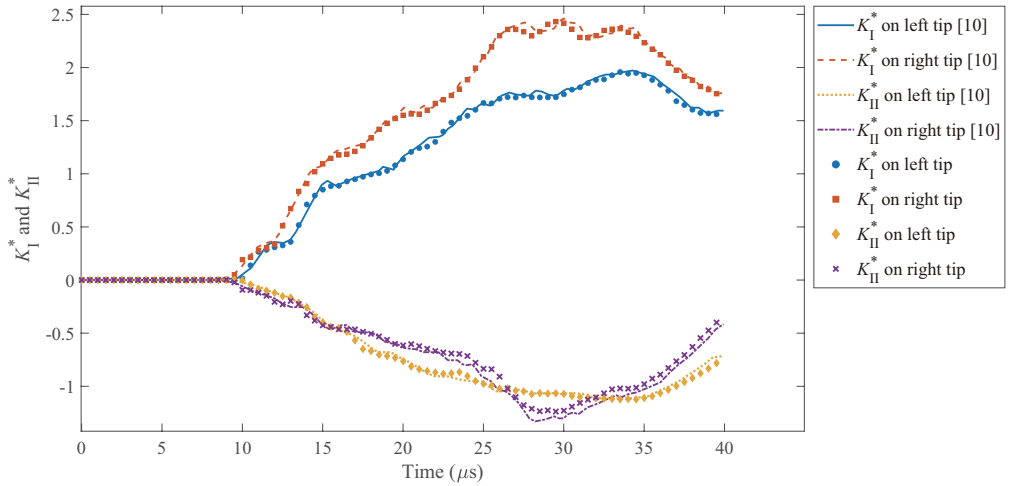

Figure 15: Comparison of mixed-mode DSIFs.

sidering the crack propagation, the material average schemes do not have obvious influence on mode-I SIF results. Then the dynamic behaviors of FGM plates with horizontally oriented and slant cracks are discussed with respect to different variation of material gradients. Finally, the mixed-mode DSIFs on hole plate is numerically evaluated. The OSPD solutions in these numerical studies are compared with reference solutions in the literature. Good agreements can be obtained in the calculation of mode-I SIFs and DISFs, which shows the accuracy and reliability of OSPD.

However, due to the limitation of current OSPD formulation, there is a relatively low accuracy in mode-II fracture evaluation of FGM. Therefore, in future studies, it is necessary to modify and optimize the OSPD to accurately capture and simulate the shearing behaviour of local failure. The proposed method in this article provides an alternative perspective in the fracture analysis of FGM, which may have promising applications in computing technologies and engineering designs.

References

[1] Koizumi M. FGM activities in Japan. Composites Part B: Engineering 1997;28(1-2):1-4.

[2] Chu C, Zhu J, Yin Z, Wang S. Hydroxyapatite-Ti functionally graded

biomaterial fabricated by powder metallurgy. Materials Science and Engineering: A 1999;271(1-2):95-100.

[3] Medvedovski E. Ballistic performance of armour ceramics: Influence of design and structure. Part 1. Ceramics International 2010;36(7):2103-2115.

[4] Marin L. Numerical solution of the Cauchy problem for steady-state heat transfer in two-dimensional functionally graded materials. International Journal of Solids and Structures 2005;42(15):4338-4351.

[5] Erdogan F, Wu BH. The surface crack problem for a plate with functionally graded properties. ASME Journal of Applied Mechanics 1997;64(3):449-456.

[6] Zhong Z, Cheng Z. Fracture analysis of a functionally graded strip with arbitrary distributed material properties. International Journal of Solids and Structures 2008;45(13):3711-3725.

[7] Shodja HM, Ghahremaninejad A. An FGM coated elastic solid under thermomechanical loading: a two dimensional linear elastic approach. Surface and Coatings Technology 2006;200(12-13):4050-4064.

[8] Guo LC, Noda N. Fracture mechanics analysis of functionally graded layered structures with a crack crossing the interface. Mechanics of Materials 2008;40(3):81-99.

[9] Yao XF, Xu W, Bai SL, Yeh HY. Caustics analysis of the crack initiation and propagation of graded materials. Composites Science and Technology 2008;68(3-4):953-962.

[10] Song SH, Paulino GH. Dynamic stress intensity factors for homogeneous and smoothly heterogeneous materials using the interaction integral method. International Journal of Solids and Structures 2006;43(16):4830-4866.

[11] Anlas G, Santare MH, Lambros J. Numerical calculation of stress intensity factors in functionally graded materials. International Journal of Fracture 2000;104(2):131-143.

[12] Kim JH, Paulino GH. Finite element evaluation of mixed mode stress intensity factors in functionally graded materials. International Journal for Numerical Methods in Engineering 2002;53(8):1903-1935.

[13] Zhang C, Savaidis A, Savaidis G, Zhu H. Transient dynamic analysis of a cracked functionally graded material by a BIEM. Computational Materials Science 2003;26:167-174.

[14] Dolbow JE, Gosz M. On the computation of mixed-mode stress intensity factors in functionally graded materials. International Journal of Solids and Structures 2002;39(9):2557-2574.

[15] Sladek J, Sladek V, Zhang C. A meshless local boundary integral equation method for dynamic anti-plane shear crack problem in functionally graded materials. Engineering Analysis with Boundary Elements 2005;29(4):334-342.

[16] Sladek J, Sladek V, Zhang C. An advanced numerical method for computing elastodynamic fracture parameters in functionally graded materials. Computational Materials Science 2005;32(3-4):532-543.

[17] Dai KY, Liu GR, Lim KM, Han X, Du SY. A meshfree radial point interpolation method for analysis of functionally graded material (FGM) plates, Computational Mechanics 2004;34(3):213-223.

[18] Bui TQ, Nguyen NT, Nguyen MN, Truong TT. Analysis of transient dynamic fracture parameters of cracked functionally graded composites by improved meshfree methods. Theoretical and Applied Fracture Mechanics 2018;96:642-657.

[19] Thai CH, Do VN, Nguyen-Xuan H. An improved Moving Kriging-based meshfree method for static, dynamic and buckling analyses of functionally graded isotropic and sandwich plates. Engineering Analysis with Boundary Elements, 2016;64:122-136.

[20] Imachi M, Tanaka S, Bui TQ. Mixed-mode dynamic stress intensity factors evaluation using ordinary state-based peridynamics. Theoretical and Applied Fracture Mechanics 2018;93:97-104.

[21] Dai MJ, Tanaka S, Oterkus S, Oterkus E. Mixed-mode stress intensity factors evaluation of flat shells under in-plane loading employing

ordinary state-based peridynamics. Theoretical and Applied Fracture Mechanics 2021;112:102841.

[22] Dai MJ, Tanaka S, Bui TQ, Oterkus S, Oterkus E. Fracture parameter analysis of flat shells under out-of-plane loading using ordinary state-based peridynamics. Engineering Fracture Mechanics 2021;244:107560.

[23] Dai MJ, Tanaka S, Guan PC, Oterkus S, Oterkus E. Ordinary state-based peridynamic shell model with arbitrary horizon domains for surface effect correction. Theoretical and Applied Fracture Mechanics 2021;115:103068.

[24] Dai MJ, Tanaka S, Oterkus S, Oterkus E. Static and dynamic mechanical behaviors of cracked Mindlin plates in ordinary state-based peridynamic framework. Acta Mechanica 2022;233:299-316.

[25] Ozdemir M, Kefal A, Imachi M, Tanaka S, Oterkus E. Dynamic fracture analysis of functionally graded materials using ordinary state-based peridynamics. Composite Structures 2020;244:112296.

[26] Yang Z, Oterkus E, Oterkus S. Peridynamic formulation for higher order functionally graded beams. Thin-Walled Structures 2021;160:107343.

[27] Silling SA. Reformulation of elasticity theory for discontinuities and long-range forces. Journal of the Mechanics and Physics of Solids 2000;48(1):175-209.

[28] Zhang H, Qiao P. Virtual crack closure technique in peridynamic theory. Computer Methods in Applied Mechanics and Engineering 2020;372:113318.

[29] Ha YD, Bobaru F. Studies of dynamic crack propagation and crack branching with peridynamics. International Journal of Fracture 2010;162(1):229-244.

[30] Bobaru F, Duangpanya M. The peridynamic formulation for transient heat conduction. International Journal of Heat and Mass Transfer 2010;53(19-20):4047-4059.

[31] Silling SA, Askari E. A meshfree method based on the peridynamic model of solid mechanics. Computers & Structures 2005;83(17-18):1526-1535.

[32] Silling SA, Epton M, Weckner O, Xu J, Askari E. Peridynamic states and constitutive modeling. Journal of Elasticity 2007;88(2):151-184.

[33] Madenci E, Oterkus E. Peridynamic Theory and Its Applications. New York: Springer; 2014.

[34] Ŝolín P. Partial differential equations and the finite element method (Vol. 73). New Jersey: John Wiley & Sons; 2005.

[35] Causon DM, Mingham CG. Introductory finite difference methods for PDEs. London: Mingham & Ventus Publishing ApS; 2010.

[36] Coleman CJ, Tullock DL, Phan-Thien N. An effective boundary element method for inhomogeneous partial differential equations. Zeitschrift für angewandte Mathematik und Physik ZAMP 1991;42(5):730-745.

[37] Madenci E, Barut A, Futch M. Peridynamic differential operator and its applications. Computer Methods in Applied Mechanics and Engineering 2016;304:408-451.

[38] Madenci E, Dorduncu M, Barut A, Futch M. Numerical solution of linear and nonlinear partial differential equations using the peridynamic differential operator. Numerical Methods for Partial Differential Equations 2017;33(5):1726-1753.

[39] Wang H, Tanaka S, Oterkus S, Oterkus E. Evaluation of stress intensity factors under thermal effect employing domain integral method and ordinary state based peridynamic theory. Continuum Mechanics and Thermodynamics 2021.

[40] Madenci E, Barut A, Dorduncu M. Peridynamic differential operator for numerical analysis. Gewerbestrasse: Springer; 2019.

[41] Wang H, Oterkus E, Oterkus S. Predicting fracture evolution during lithiation process using peridynamics. Engineering Fracture Mechanics 2018;192:176-191.

[42] Wang H, Oterkus E, Oterkus, S. Three-dimensional peridynamic model for predicting fracture evolution during the lithiation process. Energies 2018;11(6):1461.

[43] Rahimi MN, Kefal A, Yildiz M. An improved ordinary-state based peridynamic formulation for modeling FGMs with sharp interface transitions. International Journal of Mechanical Sciences 2021;197:106322.

[44] Oterkus S, Madenci E, Agwai A. Peridynamic thermal diffusion. Journal of Computational Physics 2014;265:71-96.

[45] Mitts C, Naboulsi S, Przybyla C, Madenci E. Axisymmetric peridynamic analysis of crack deflection in a single strand ceramic matrix composite. Engineering Fracture Mechanics 2020;235:107074.

[46] Behera D, Roy P, Madenci E. Peridynamic modeling of bonded-lap joints with viscoelastic adhesives in the presence of finite deformation. Computer Methods in Applied Mechanics and Engineering 2021;374:113584.

[47] Nguyen HA, Wang H, Tanaka S, Oterkus S, Oterkus E. An in-depth investigation of bimaterial interface modeling using ordinary state-based peridynamics. Journal of Peridynamics and Nonlocal Modeling 2021.

[48] Rice JR. A path independent integral and the approximate analysis of strain concentration by notches and cracks. ASME Journal of Applied Mechanics 1968;35(2):379-386.

[49] Stern M, Becker EB, Dunham RS. A contour integral computation of mixed-mode stress intensity factors. International Journal of Fracture 1976;12(3):359-368.

[50] Yau JF, Wang SS, Corten HT. A mixed-mode crack analysis of isotropic solids using conservation laws of elasticity. ASME Journal of Applied Mechanics 1980;47(2):335-341.

[51] Yu H, Wu L, Guo L, Du S, He Q. Investigation of mixed-mode stress intensity factors for nonhomogeneous materials using an interaction integral method. International Journal of Solids and Structures 2009;46(20):3710-3724.

[52] Chen J, Wu L, Du S. A modified J integral for functionally graded materials. Mechanics Research Communications 2000;27(3):301-306.

[53] Raju IS, Shivakumar KN. An equivalent domain integral method in the two-dimensional analysis of mixed mode crack problems. Engineering Fracture Mechanics 1990;37(4):707-725.

[54] William ML. On the stress distribution at the base of a stationary crack. ASME Journal of Applied Mechanics 1957:24:109-114

[55] Anderson TL. Fracture mechanics: fundamentals and applications. Boca Raton: CRC press; 2017.

[56] Kilic B, Madenci E. An adaptive dynamic relaxation method for quasi-static simulations using the peridynamic theory. Theoretical and Applied Fracture Mechanics 2010;53(3):194-204.

[57] Konda N, Erdogan F. The mixed mode crack problem in a nonhomogeneous elastic medium. Engineering Fracture Mechanics 1994;47(4):533-545.